Tropical Atlantic stratification response to late Quaternary precessional forcing

R.A. Nascimento, I.M. Venancio, C.M. Chiessi, J.M. Ballalai, H. Kuhnert, H. Johnstone, T.P. Santos, M. Prange, A. Govin, S. Crivellari, et al.

Tropical Atlantic stratification response to late Quaternary precessional forcing

Nascimento, R. A[1*]; Venancio, I. M.[1,2]; Chiessi, C. M.[3]; Ballalai, J. M.[1]; Kuhnert, H.[4]; Johnstone, H.[4]; Santos, T. P. [1]; Prange, M.[4]; Govin, A.[5]; Crivellari, S.[3]; Mulitza, S.[4]; Albuquerque, A. L. S.[1]

[1] Programa de Geociências (Geoquímica), Universidade Federal Fluminense, Niterói, Brazil

[2] Center for Weather Forecasting and Climate Studies (CPTEC), National Institute for Space Research (INPE), Cachoeira Paulista, Brazil

[3] School of Arts, Sciences and Humanities, University of São Paulo, São Paulo, Brazil

[4] MARUM - Center for Marine Environmental Sciences, University of Bremen, Bremen, Germany

[5] Laboratoire des Sciences du Climat et de l'Environnement/Institut Pierre Simon Laplace, CEA-CNRS-UVSQ, Université Paris Saclay, Gif sur Yvette, France

*Corresponding author
e-mail address: rodrigoan@id.uff.br

Keywords: southwestern tropical Atlantic stratification; precession; ITCZ; South Atlantic Subtropical Gyre; cross-equatorial heat transport

Abstract

The upper ocean circulation in the western tropical Atlantic (WTA) is responsible for the northward cross-equatorial heat transport as part of the Atlantic Meridional Overturning Circulation (AMOC). This cross-equatorial transport is influenced by the thermocline circulation and stratification. Although seasonal thermocline stratification in the WTA is precession-driven, the existence of an orbital pacemaker of changes in the entire WTA upper ocean stratification, which comprises the main thermocline, remains elusive. Here, we present a 300 ka-long record of the WTA upper ocean stratification and main thermocline temperature based on oxygen isotopes ($\delta^{18}O$) and Mg/Ca of planktonic foraminifera. Our $\Delta\delta^{18}O$ record between *Globigerinoides ruber* and *Globorotalia truncatulinoides*, representing upper ocean stratification, shows a robust precession pacing, where strong stratification was linked to high summer insolation in the Northern Hemisphere (precession minima). Mg/Ca-based temperatures support that stratification

is dominated by changes in thermocline temperature. We present a new mechanism to explain changes in WTA stratification, where during the Northern Hemisphere summer insolation maxima, the Intertropical Convergence Zone shifts northward, developing a negative wind stress curl anomaly in the tropical Atlantic. This, in turn, pulls the main thermocline up and pushes the South Atlantic Subtropical Gyre southwards, increasing the stratification to the north of the gyre. This mechanism is supported by experiments performed with the Community Earth System Model (CESM1.2). Finally, we hypothesize that the precession-driven WTA stratification may affect the cross-equatorial flow into the North Atlantic.

1. Introduction

The tropics play a major role in the Earth's climate system (Berger et al. 2006; Rutherford and D'Hondt, 2000; McIntyre and Molfino 1996). In this area, trade winds connect the circulation of the lower atmosphere to that of the ocean surface. The upper ocean circulation in the western tropical Atlantic (WTA) is responsible for the northward-cross-equatorial transport of heat and salt as part of the upper limb of the Atlantic Meridional Overturning Circulation (AMOC) (Zhang et al. 2011; Hazeleger and Drijfhout 2006; Lumpkin and Speer 2003). Most of this transport occurs within the thermocline (Schott et al. 2005; Schott et al. 1998). Instrumental data and model experiments suggest that deep-water formation at the high latitudes of the North Atlantic is linked to the water volume transported northwards within the WTA (Zhang et al. 2011; Vellinga and Wu, 2004; Yang, 1999). Venancio et al. (2018) suggested that WTA thermocline stratification, directly influenced by trade wind stress, affects the water transport towards the North Atlantic during millennial-scale North Atlantic cold-events. Meanwhile, Kaiser et al. (2019) recently reported precessional modulated changes in cross-equatorial water transport during the mid-Pleistocene. Therefore, it is plausible that orbital variations in trade winds pattern and WTA upper ocean hydrography have implications for cross-equatorial transport and AMOC strength.

On orbital timescales, variations in low latitude insolation are primarily driven by precession (Clement et al. 2004; Berger et al. 1993). Precession-forced variability of trade wind zonality has been documented in the tropical Atlantic (Wolff et al. 1999; McIntyre and Molfino 1996; Molfino and McIntyre 1990; McIntyre et al. 1989). This was linked to variations in the intensity of the West African monsoon (COHMAP et al. 1988; McIntyre et al. 1989; Molfino and McIntyre 1990; McIntyre and Molfino 1996), which in turn is modulated by boreal summer insolation (Skonieczny et al. 2019; Kutzbach and Liu, 1997; Kutzbach and Guetter, 1986; Kutzbach and Otto-Bliesner, 1982). Changes in trade wind zonality control tropical Atlantic stratification by changing the depth of the shallow seasonal thermocline with a precession beat (Venancio et al. 2018; McIntyre and Molfino et al. 1996; Molfino and McIntyre, 1990; McIntyre et al. 1989). However, the seasonal thermocline comprises only the thin uppermost portion of the main thermocline.

The main thermocline is ventilated at midlatitudes primarily by buoyancy flux and westerlies-driven Ekman pumping (Sprintall and Tomczak, 1993; Luyten et al. 1983a). The amount of water advected towards low latitudes in the main thermocline depends on the strength of the midlatitude westerlies (Luyten et al. 1993b), while the properties of the main thermocline waters are largely influenced by characteristics of the ocean surface in the formation region (Poole and Tomczak, 1999; Sprintall and Tomczak, 1993). Orbitally-driven changes in the Southern Hemisphere westerlies are primarily controlled by obliquity forcing on the meridional temperature gradient at midlatitudes (Timmermann et al. 2014; Mantsis et al. 2014; Mantsis et al. 2011). Consequently, the obliquity signal imprinted in midlatitudes can be propagated within the main thermocline towards the WTA. However, the existence of an orbital pacemaker of changes in the main thermocline density structure and hence in the WTA upper ocean stratification remains elusive.

To investigate the response of the WTA upper ocean stratification to orbital forcing and its possible implications for the interhemispheric transport of heat and salt, we present a millennial resolution 300 ka-long record of $\Delta\delta^{18}O$ between surface- and

deep-dwelling planktonic foraminifera species ($\delta^{18}O_{Globorotalia\ truncatulinoides}$ - $\delta^{18}O_{Globigerinoides\ ruber}$). In addition, we present a record of main thermocline temperatures based on Mg/Ca ratios of *Globorotalia truncatulinoides*, as well as seawater-$\delta^{18}O$ corrected for changes in ice-volume ($\delta^{18}O_{sw\text{-}ivc}$), a proxy for relative changes in main thermocline salinity. Samples come from sediment core GL-1180 collected off eastern Brazil (8° 27'18" S, 33° 32'53" W, 1037 m water depth) (Fig. 1). Our results show that WTA upper ocean stratification is coupled to precession, particularly during periods of high eccentricity. We propose a new mechanism to explain changes in WTA stratification, which is corroborated by results from the Community Earth System Model (CESM1.2). Finally, we hypothesize a connection between WTA stratification and interhemispheric oceanic transport on orbital timescales.

2. Regional Setting

Upper ocean circulation in the WTA is marked by the bifurcation of the southern branch of the South Equatorial Current (sSEC). The sSEC bifurcates between 10 and 14°S (Rodrigues et al. 2007), giving rise to the southward flowing Brazil Current and the northward flowing North Brazil Undercurrent (NBUC)/North Brazil Current (NBC) (Fig. 1) (Stramma and England 1999). The NBUC/NBC are part of the upper limb of the AMOC (Zhang et al. 2011; Hazeleger and Drijfhout 2006). At ~8°S, sediment core GL-1180 is sensitive to variations in the latitude of the sSEC bifurcation. The sSEC represents the northernmost boundary of the warm and saline South Atlantic Subtropical Gyre (SASG) (Marcelo et al. 2018; Rodrigues et al. 2007; Stramma, 1991), which is clearly marked in temperature at 250 m water depth (Fig. 1). North of the SASG, the thermocline is shallow due to equatorial divergence forced by the trade winds pushing waters at the Ekman layer from the equator towards the subtropics. South of the SASG gyre, the westerlies force the Ekman transport in the opposite direction. This convergence pumps warm surface waters downward and pushes the thermocline down, forming a thick upper ocean layer of warm waters, namely the SASG (Fig 1).

The mean sea surface temperature and salinity at site GL-1180 are 27.7°C and 36.3, respectively (Locarnini et al. 2013; Zweng et al. 2013). At 250 m water depth, in the main thermocline, temperature and salinity are 12.1°C and 35.1, respectively (Locarnini et al. 2013). Tropical Water is present in the upper 100 m of the water column, South Atlantic Central Water (SACW) between 100 and 500 m water depth, and Antarctic Intermediate Water from 500 to 1200 m water depth (Stramma and England, 1999). The SACW, the water mass of the South Atlantic main thermocline, is subducted at the South Atlantic Subtropical Front (Stramma and England, 1999; Poole and Tomczak, 1999).

Figure 1.

One of the key atmospheric features of the tropics is the Intertropical Convergence Zone (ITCZ), the belt of deep convection located between the Hadley cells of both hemispheres (Schneider et al. 2014). Due to the seasonal asymmetry in the interhemispheric heat budget, the ITCZ migrates southward (northward) during austral summer (winter) (Marshal et al. 2014; Schneider et al. 2014). In the South Atlantic, the SE trade winds and the lower limb of Southern Hemisphere Hadley cell are weaker (stronger) during the austral summer (winter). Furthermore, during austral summer (winter), an anticyclonic atmospheric circulation expands towards the equator in the WTA (Rodrigues et al. 2007). The opposite occurs during austral winter when a cyclonic circulation expands southwards over the continental margin of northeastern Brazil. The variation between atmospheric anticyclonic and cyclonic circulation, and hence positive and negative wind stress curl respectively, controls the position of the sSEC bifurcation, causing its southward (northward) shift during austral winter (summer) (Rodrigues et al. 2007).

3. Material and methods

3.1. Sediment core GL-1180

We investigate the 1732 cm-long marine sediment core GL-1180 provided by Petrobras. Visual analysis of the core does not indicate any sedimentation disturbance. Sediment samples of approximately 10 cm^3 were taken every 2 cm. For the chemical analyses described below, all sediment samples were wet-sieved to retain the fraction larger than 63 μm. The retained material was dried at 50 °C for 24 hours and stored in acrylic flasks. Foraminifera shells were handpicked using a binocular microscope.

3.2. Age model

The age model of GL-1180 is based on six radiocarbon ages (Supporting Information, Table S1) and the visual alignment of the benthic $\delta^{18}O$ record of *Cibicidoides sp.* (see section 3.3) with a global $\delta^{18}O$ stack. For radiocarbon dating, 6 to 10 mg of *Globigerinoides ruber* and *Trilobatus sacculifer* shells were selected from the size fraction larger than 150 μm (Table S1). Analyses were performed at the Beta Analytic Radiocarbon Dating Laboratory (Miami, USA) using accelerator mass spectrometry. Radiocarbon ages were calibrated using the IntCal13 calibration curve (Reimer et al. 2013) with a reservoir effect of 400 ± 200 without additional local reservoir effect. For the benthic $\delta^{18}O$ alignment, the LR04 global $\delta^{18}O$ stack was used (Lisiecki and Raymo, 2005) (Fig. S1 and Table S2 in the Supporting Information). Alignment uncertainties were calculated following Govin et al. (2015). The final age model (Fig. S1) was constructed using the software Bacon v 2.3 (Blaauw and Christen, 2011).

3.3. Isotopic analysis from core GL-1180 and $\Delta\delta^{18}O$ calculation

For isotopic analyses, ten shells of *Cibicidoides sp.* (300-350 μm), *G. ruber* (white, *sensu lato*, 250-300 μm), and *Globorotalia truncatulinoides* (dextral, 300-425 μm) were handpicked. Although *G. truncatulinoides* $\delta^{18}O$ shows a positive correlation with shell size (Birch et al. 2013; Elderfield et al. 2002), $\delta^{18}O$ variation is minimal in shells larger than 250 μm (Birch et al. 2013). The sampling resolution of benthic foraminifera $\delta^{18}O$ was 4 cm (373 samples). The planktonic foraminifera sampling resolution varied

between 4 and 2 cm for *G. ruber* and *G. truncatulinoides,* totaling 507 and 509 samples, respectively.

Analyses of $\delta^{18}O$ of benthic foraminifera were carried out at the Center for Marine Environmental Sciences (MARUM), University of Bremen (Bremen, Germany) using a Finnigan MAT 251 isotope ratio mass spectrometer (IRMS) equipped with an automated carbonate preparation device type Kiel I. The standard deviation of the in-house standard was 0.03 ‰. Analyses of planktonic foraminifera $\delta^{18}O$ were performed at the Paleoceanography and Paleoclimatology Laboratory (P2L), University of São Paulo (São Paulo, Brazil) using a Thermo Scientific MAT 253 IRMS coupled to a Thermo Scientific Kiel IV automated carbonate preparation device. The standard deviation of the in-house standard SHP2L (Crivellari et al. 2021) was 0.08 and 0.07 ‰ for *G. ruber* and *G. truncatulinoides*, respectively. Measurements are reported in parts per thousand relative to the Vienna Pee Dee Belemnite (VPDB) and have been normalized against repeated measurement of NBS19 standard. NBS19 standard deviation over the measurement period was 0.07 and 0.06 ‰ for *G. ruber* and *G. truncatulinoides*, respectively.

$\Delta\delta^{18}O$ resulted from calculating *G. truncatulinoides* $\delta^{18}O$ minus *G. ruber* $\delta^{18}O$ from the same sample (depth). Changes in $\delta^{18}O$ recorded by one or both foraminifera species result from temperature or salinity variations of the surrounding seawater, which ultimately can affect the $\Delta\delta^{18}O$. Since temperature and salinity control the density of seawater, high (low) $\Delta\delta^{18}O$ values indicate increased (reduced) upper ocean stratification between the mixed layer and the main thermocline. To remove any linear trend from the $\Delta\delta^{18}O$ record, we used the detrending function of the software MATLAB.

3.4. Mg/Ca analyses from the core GL-1180

For Mg/Ca analyses, between 8 and 20 shells of *G. truncatulinoides* (dextral, 300-425 µm) were handpicked. The cleaning protocol of the *G. truncatulinoides* shells for Mg/Ca analyses followed Barker et al. (2003). Each sample was cleaned with water, methanol, and a hot hydrogen peroxide solution; with no reductive cleaning step. After

198 cleaning, samples were dissolved in dilute HNO_3. Mg/Ca analyses of *G. truncatulinoides*
199 were performed at the MARUM using an inductively coupled plasma optical emission
200 spectrometer (ICP-OES) (Agilent Technologies, 700 Series) with an autosampler (ASX-
201 520 Cetac). Fe, Mn, and Al were measured in addition to Ca and Mg. Three replicates
202 of each sample were measured, and their average was used. The calibration series
203 consisted of one blank and five multi-element standards containing between 20 and 80
204 ppm of Ca prepared from a mixed standard purchased from SCP Science, France
205 (Mg/Ca of 4.17 mmol/mol). All samples were within the calibrated concentration range.
206 An in-house standard (Mg/Ca = 2.96 mmol mol^{-1}), as well as the standards ECRM 752-
207 1 (Bureau of Analysed Standards, Great Britain) and Reinstoff Nr. 3 (Bundesanstalt für
208 Materialforschung und –Prüfung, Germany), were used to verify the accuracy of the
209 measurements and to allow inter-laboratory comparison. The in-house standard was
210 measured every 5 samples, while the other standards were measured every ~90
211 samples. The standard deviations of the in-house standard, ERCM 752-1 and Reinstoff
212 Nr. 3 were 0.02 mmol mol^{-1} (0.54%, n = 113), 0.02 mmol mol^{-1} (0.47%, n = 8), and 0.01
213 mmol mol^{-1} (0.70%, n = 8), respectively. Samples with Al/Ca ratio higher than 0.2 mmol
214 mol^{-1} or having Mg/Ca values outside of 4 σ of the mean (σ = 0.20 mmol mol^{-1}) were
215 discarded (four out of 406). The average Al/Ca ratio was 0.02 mmol mol^{-1}. There was no
216 correlation between Mg/Ca and Al/Ca (R^2 = 0.03), Mn/Ca (R^2 = 0.13), and Fe/Ca (R^2 =
217 0.001).

218 Temperature was calculated based on the species-specific equation for *G.*
219 *truncatulinoides* by Regenberg et al. (2009) (r = 0.59) with an accuracy estimation of ±
220 2°C. This equation was chosen due to the following reasons: (1) it was established based
221 on tropical Atlantic top-cores; (2) the size of foraminifera shells used by the authors has
222 a similar range to the shells analyzed here; (3) the same cleaning protocol was used,
223 also without a reductive step.

3.5. Calculation of seawater and foraminifera $\delta^{18}O$ corrected by changes in ice-volume

To calculate the ice-volume-corrected seawater $\delta^{18}O$ ($\delta^{18}O_{sw\text{-}ivc}$), we used the isotopic paleotemperature equation of Shackleton (1974) following Regenberg et al. (2009). For practical comparison between Vienna Standard Mean Ocean Water (VSMOW) and VPDB we apply an offset of 0.27‰ (Hut, 1987). The temperature component was removed using the Mg/Ca-derived temperatures. The ice-volume effect was removed using the sea level stack of Spratt and Lisiecki (2016), which chronology is based on the LR04 global $\delta^{18}O$ stack (Lisiecki and Raymo, 2005). The ± 2°C uncertainty of Mg/Ca-based temperatures (Regenberg et al. 2009) is equivalent to a change of ~0.5 ‰ in $\delta^{18}O$. The standard deviation for *G. truncatulinoides* $\delta^{18}O$ measurements is ± 0.07 ‰, and the propagated cumulative root-mean-square error calculated for the $\delta^{18}O_{sw\text{-}ivc}$ is ± 0.5 ‰ (in other words, the analytical error for foraminiferal $\delta^{18}O$ determinations is negligible here).

We used the same sea level stack (Spratt and Lisiecki 2016) to remove the ice-volume effect from *G. ruber* and *G. truncatulinoides* $\delta^{18}O$ records ($\delta^{18}O_{ivc}$). We used $\delta^{18}O_{ivc}$ of planktonic foraminifera in order to perform spectral analysis of $\delta^{18}O$ records without high latitude orbital components related to ice-volume changes.

3.6. Spectral analysis

REDFIT analyses (Schulz & Mudelsee, 2002) were performed using the software PAST (Hammer et al., 2001) in order to determine the statistically significant periodicities present in our records. We performed the analysis using four segments tapered with a Hanning spectral window. Tests with different numbers of segments did not change the significance of the main frequencies, suggesting that they are a robust feature of our records. To avoid excessive interpolation, we did not perform spectral analysis on

Mg/Ca-based thermocline temperature since this record presents some gaps over the last 300 ka.

3.7. Atmospheric modeling

To study the effect of precession on tropical winds over the Atlantic, we performed two experiments using the general circulation model CESM1.2. The state-of-the-art atmosphere model component CAM5 runs with 1.9° x 2.5° horizontal resolution (finite volume core) and with 30 vertical levels. Standard pre-industrial boundary conditions were used except for the orbital parameters, which have been set to Quaternary mean values for eccentricity (0.03) and obliquity (23.4°). In the two experiments, precession was set to its extreme values (90° and 270° longitude of perihelion relative to the moving vernal equinox minus 180°), which reflect maximum (aphelion at boreal summer solstice, i.e., minimum boreal summer insolation) and minimum (perihelion at boreal summer solstice, i.e., maximum boreal summer insolation) precession, respectively. Both experiments, named P_min (minimum precession) and P_max (maximum precession), run for 250 years. Annual means were calculated from the last 50 years of each experiment. Both experiments were initialized with observational ocean data (Steele et al., 2001). Because of the short integration time (due to limited computational resources), the simulations provide no meaningful information about subsurface ocean conditions or deep-ocean circulation changes. We therefore point out that our model experiments are only focusing on changes in atmosphere dynamics under two extreme precessional configurations.

4. Results

4.1. Geochemical proxies

Our planktonic $\delta^{18}O$ records span the last three glacial-interglacial cycles (300 ka). The *G. ruber* $\delta^{18}O$ values vary between -1.70 and 0.67‰ and shows a clear glacial-

interglacial pattern. In contrast, the *G. truncatulinoides* $\delta^{18}O$ record, which varies between 0.34 and 2.40 ‰ (Fig. 2), presents more pronounced variability, particularly during MIS7 and MIS5. The apparent calcification depth (ACD) of the chosen foraminifera species is ~80 m water depth for *G. ruber* and ~250 m water depth for *G. truncatulinoides* (see Text S1 and Fig. S2). A total of 468 paired $\delta^{18}O_{G.\ truncatulinoides}$-$\delta^{18}O_{G.\ ruber}$ ($\Delta\delta^{18}O$) values cover the last ~300 ka at a millennial-scale resolution (Fig. 2b). $\Delta\delta^{18}O$ varies between 0.80 and 3.70 ‰. Most of our $\Delta\delta^{18}O$ record parallels precession (Fig. 2b).

Here we provide, an almost continuous, Mg/Ca-based temperature record of the WTA main thermocline spanning the last 300 ka. The *G. truncatulinoides* Mg/Ca record from sediment core GL-1180 varies between 1.59 to 2.85 mmol/mol. The mean Mg/Ca-based thermocline temperature is 9.4°C ranging between 3.4 and 15.4°C (Fig. 2c). In the core-top sample, the Mg/Ca-based temperature is 12.6°C, similar to modern temperature at 250 m water depth (11.6 °C, Locarnini et al., 2013), which is the calculated ACD of *G. truncatulinoides*. The $\delta^{18}O_{sw\text{-}ivc}$ record (Fig. 2d) vary from -2.05 to 1.42 ‰ and is strongly coupled with the temperature variations. Thermocline temperatures and $\Delta\delta^{18}O$ are inversely related, with increased thermocline temperatures corresponding to decreased $\Delta\delta^{18}O$ values and thus reduced upper ocean stratification (Fig. 2c).

4.2. Time-series analyses

The frequency spectra of *G. truncatulinoides* $\delta^{18}O$ corrected for changes in ice-volume ($\delta^{18}O_{ivc}$) shows a dominance of precession forcing (~23 ka) (Fig. 3a), while *G. ruber* $\delta^{18}O_{ivc}$ is dominated by 100 ka periodicity (~88 ka) (Fig. 3b). The frequency spectrum of $\Delta\delta^{18}O$ shows a robust signal at the precessional band, with a pronounced peak at 22 ka (Fig. 3c). Secondary peaks in the $\Delta\delta^{18}O$ frequency spectrum (at 95% level) are close to the obliquity and eccentricity bands. Moreover, a peak at 12-13 ka can be observed in the *G. truncatulinoides* $\delta^{18}O_{ivc}$ and $\Delta\delta^{18}O$ records. REDFIT analyses in non-

ice-volume-corrected $\delta^{18}O$ records of both foraminifera species indicate the dominance of 100 ka periodicity (Fig. S3).

4.3. Climate model outputs

When forced by maximum and minimum precession, our CESM 1.2 experiments show differences in the annual-average trade winds pattern, ITCZ position, and wind stress curl over the tropical Atlantic when forced by maximum and minimum precession. The climate model results show anomalously strong annual-mean SE trade winds over the tropical Atlantic in experiment P_min relative to P_max (Fig. 4a), while the annual-mean northeastern trade winds were weakened. This agrees with the annual-average northward shift of the ITCZ system and strengthening of the West African monsoon in experiment P_min relative to P_max (Fig. 4b). As a result of the northward shift of the ITCZ system under minimum precession, a large-scale negative wind stress curl anomaly develops in the tropical Atlantic from approximately 10°N to 15°S (Fig. 4a). In the Southern Hemisphere, negative wind stress curl is linked to the divergence of waters at the Ekman layer, resulting in a region of Ekman suction (cyclonic circulation). Therefore, anomalous negative wind stress curl would mean a weakened Ekman pumping or enhanced suction. The latter is mostly the case for the equatorial and tropical South Atlantic since this region is already dominated by a cyclonic circulation. In the South Atlantic, an anomalous positive wind stress curl forces an enhanced anticyclonic circulation to the south of 15°S. The annual averaged zero wind stress curl line at the limit between the tropical cyclonic and subtropical anticyclonic circulation in the South Atlantic is displaced southward during minimum precession due to the expansion of the cyclonic circulation in the tropical Atlantic.

Figure 2.

Figure 3.

Figure 4.

5. Discussion

5.1. Precessional signal in the western tropical Atlantic

Following previous studies (Venancio et al. 2018; Mulitza et al. 1997), high (low) values of $\Delta\delta^{18}O$ calculated between deep- and shallow-dwelling foraminiferal $\delta^{18}O$ are interpreted as increased (reduced) upper ocean stratification (Fig. 2b). In general, increased (reduced) WTA stratification fits remarkably with minimum (maximum) precession (Figs. 2b, 3c). This strongly suggests that precession forcing modulated the WTA upper ocean stratification over the late Pleistocene. The amplitude of $\Delta\delta^{18}O$ variations is noticeably increased during periods of high eccentricity (Fig. 2b), highlighting the modulating effect of eccentricity on the amplitude of precession changes, and hence on the amplitude of our $\Delta\delta^{18}O$ record. The influence of obliquity on stratification is also indicated by our $\Delta\delta^{18}O$ frequency spectrum (Fig. 3c). This could be caused by obliquity-forced variations in the meridional temperature gradient, affecting the Southern Hemisphere westerlies (Mantsis et al. 2014; Timmermann et al. 2014; Mantsis et al. 2011) and the Ekman pumping at midlatitudes, eventually transporting the obliquity signal towards the tropical Atlantic via SACW. However, no evidence of an obliquity signal is observed in the frequency spectrum of *G. truncatulinoides* $\delta^{18}O_{ivc}$ (Fig. 3). Alternatively, obliquity-forced fluctuations in the meridional temperature gradient could affect the intensity of the southeastern trade winds, causing variations in the WTA mixed layer temperature due to changes in wind stress (Hou et al. 2020). This mechanism potentially imprinted the obliquity signal in the WTA ocean surface.

We observe a peak centered at 12 and 13 ka in our $\Delta\delta^{18}O$ and *G. truncatulinoides* $\delta^{18}O_{ivc}$ frequency spectra, respectively (Fig. 3a, c). This period is consistent with the half-precession cycle (11.5 ka) found in the intertropical belt (Berger and Loutre, 1997; Berger

356 at al. 2006) and with results from previous paleoceanographic studies in the WTA
357 (Venancio et al. 2018; Niemitz and Billups 2005). In the intertropical zone, the sun passes
358 overhead twice a year (at the equinoxes). Over a precession cycle, this produces two
359 peaks of insolation maxima and the half-precession component (Rutherford and
360 D'Hondt, 2000; Berger and Loutre, 1997). Although half-precession signal decreases
361 with the distance from the equator, it can be observed in the whole intertropical belt
362 (Berger et al. 2006). Additionally, the half-precession signal can be amplified by a
363 nonlinear response of the climate system to precessional forcing on tropical insolation
364 (Hagelberg et al. 1994). Eventually, this suborbital component can be imprinted on the
365 upper ocean hydrography through changes in the atmospheric circulation dynamics.
366 Recently, a half-precession signal was identified in a stratification record from the
367 western tropical Pacific (core MD01-2386), but it was attributed to the influence of waters
368 sourced from both hemispheres (Jian et al., 2020). Although the mechanism imprinting
369 the half-precession signal to our records is not completely understood, our data imply
370 that this suborbital frequency can be found at the main thermocline in regions where
371 waters are exclusively sourced from the Southern Hemisphere.

372 The dominance of precession in $\Delta\delta^{18}O$ and *G. truncatulinoides* $\delta^{18}O_{ivc}$ indicates
373 that the dynamics of the main thermocline controls the WTA stratification. The covariation
374 between $\Delta\delta^{18}O$ and Mg/Ca-based main thermocline temperatures corroborates that the
375 WTA upper stratification mostly responds to changes in the thermal structure of the main
376 thermocline (Fig. 2c). High (low) $\Delta\delta^{18}O$ values reflecting high (low) stratification are
377 generally related to low (high) thermocline temperatures. The convergence between
378 these two independent geochemical methods (stable isotopes and Mg/Ca-based
379 temperature) supports that our $\Delta\delta^{18}O$ values indeed record changes in upper ocean
380 stratification, mostly driven by hydrographic changes in the main thermocline. The
381 spectral analysis of *G. ruber* $\delta^{18}O_{ivc}$ record (Fig. 3b) suggests that the WTA surface water
382 density was controlled by glacial-interglacial climate variability.

Between ~140 and ~120 ka thermocline temperature and $\Delta\delta^{18}O$ oscillate in opposition to the scheme described above. During this interval, the long-term variability shows that high thermocline temperature coincides with a high stratification and vice versa (Fig. 5b, c). We suggest that the cold MIS 6 glacial maximum and the warm MIS 5e interglacial changed the thermocline temperature in the opposite way to what is observed throughout most of the $\Delta\delta^{18}O$ record, dampening the temperature variability. In other words, the mechanism governing the WTA stratification through most of the record (see the section below) may have been suppressed by the glacial and interglacial boundary conditions around Termination II. The dampened temperature variability is reflected in the dominance of salinity on *G. truncatulinoides* $\delta^{18}O$. The $\delta^{18}O_{sw\text{-}ivc}$ increases by ~1.2 ‰ during Termination II (Fig. 5e). This salinity effect was possibly boosted by an increase in South Atlantic thermocline salinity at the beginning of Termination II (Fig. 5e, f) (Ballalai et al. 2019), probably due to increases in the advection of saline waters from the Indian Ocean to the South Atlantic thermocline (Scussolini et al. 2015). A decoupling between $\Delta\delta^{18}O$ and temperature is also noticed during Termination I and the Holocene (Fig 2c), which could possibly indicate a recurring feature of glacial terminations, though a further investigation would be required.

Using published *G. ruber* and *G. inflata* $\delta^{18}O$ data from sediment core GL-1090 (Santos et al. 2017a, b; Santos et al. 2020) together with new *G. inflata* $\delta^{18}O$ results from the same core, we reconstructed the upper ocean stratification in the subtropical western South Atlantic (24°S) over the last 182 ka (see Text S2 and Fig. S4). The spectral analysis of the $\Delta\delta^{18}O$ record between *G. inflata* and *G. ruber* shows an outstanding dominance of the obliquity component (Fig. S5). This result agrees with the notion that ventilation of the main thermocline in mid-latitudes is forced by the westerlies (Luyten et al. 1983a), which are modulated by obliquity (Timmermann et al. 2014). However, as indicated by the frequency spectrum of *G. truncatulinoides* $\delta 18O_{ivc}$, it is unlikely that this obliquity signal has propagated to the WTA thermocline. The frequency data strongly supports that changes in WTA stratification are primarily controlled by a precession-

paced tropical mechanism while the subtropical southwestern Atlantic is controlled by obliquity-driven mid-latitudes variability.

A $\Delta\delta^{18}O$ record from core GL-1248 calculated with $\delta^{18}O$ from *G. ruber* (white) and *Neogloboquadrina dutertrei* (Fig. S6), a species recording the seasonal thermocline, identified a precessional modulation in the stratification over the last 130 ka in the western equatorial Atlantic (see location in Fig. 1; Venancio et al. 2018). In line with the present study, the authors reasoned that strong stratification in that region was related to minimum precession. This shows that the WTA seasonal and main thermocline varied on the same orbital pace, but driven by distinct mechanisms, as discussed below.

5.2. Climate mechanism driving stratification changes in the WTA

Our $\Delta\delta^{18}O$ record shows a remarkable fit with boreal summer low latitude insolation (Fig. 6a), which is dominated by precession (Clement et al. 2004; Berger and Loutre, 1997; Berger et al. 1993). High $\Delta\delta^{18}O$ (enhanced stratification) in the WTA consistently occurs when boreal summer is close to perihelion. In fact, our $\Delta\delta^{18}O$ record reveals a coupling with the ^{230}Th-normalized Sahara dust flux, which is controlled by the precession-driven Western African Monsoon (Skonieczny et al. 2019; Fig. 6b) and with $\delta^{18}O$ of speleothems from China recording the Asian monsoon system (Cheng et al. 2016; Fig. 6c). In both cases, enhanced WTA stratification coincided with intense Northern Hemisphere monsoons. Our record is also coupled with equatorial Atlantic and eastern tropical Atlantic (ETA) divergence/stratification (McIntyre et al. 1989; Fig. 6d, e), which is controlled by WAM-driven SE trade winds zonality (McIntyre and Molfino et al. 1996; Molfino and McIntyre, 1990; McIntyre et al. 1989). Plausible mechanisms connecting Northern Hemisphere monsoon systems, ETA divergence and WTA upper-ocean stratification should comprise processes linked to the ITCZ system.

Figure 5.

Figure 6.

So far, the precession-modulated seasonal thermocline stratification in the tropical Atlantic has been ascribed to the influence of WAM-modulated SE trade winds (Venancio et al. 2018; McIntyre and Molfino, 1996). According to this explanation, the increase (decrease) in SE trade winds zonality due to a weak (strong) WAM boosts (hinders) the westward South Equatorial Current piling up warm waters in the WTA, increasing the temperature of the seasonal thermocline and weakening the stratification. This interpretation is in line with our $\Delta\delta^{18}O$ record, which shows decreased WTA stratification during precession maxima (Figure 6). However, this explanation applies to the shallow seasonal thermocline. At site GL-1180, *G. truncatulinoides* ACD is approximately 250 m water depth, recording the main thermocline. At this depth, seasonal temperature variations are negligible (Locarnini et al., 2013). Therefore, the precession-modulated piling up of warm waters in the WTA, as previously suggested (Venancio et al. 2018), is insufficient to explain our reconstructed changes, of 4-5°C, in the main thermocline temperature (Fig. 2c). Additionally, our annual average CESM1.2 experiments do not show reduced zonality of the SE trade winds due to enhanced WAM during precession minima (Fig. 4a), although it must be more evident during the boreal summer.

We suggest an alternative ocean-atmosphere mechanism that connects the dynamics of the SE trade winds to the SASG. The SASG is marked by a deep mixed layer filled with warm and saline waters, the northern extension of which is limited by the position of the sSEC (Marcelo et al. 2018; Rodrigues et al. 2007; Stramma, 1991). Towards the equator, the thermocline becomes shallower due to the equatorial divergence that brings up colder and fresher waters to the subsurface. At present, the sSEC bifurcates near the Brazilian continental margin between 10-14° S (Rodrigues et al. 2007). During the annual cycle, the sSEC bifurcation migrates latitudinally, driven by Sverdrup dynamics related to the position of the ITCZ and associated changes in the

466 wind stress curl over the ocean (Rodrigues et al. 2007). During boreal spring/summer
467 (autumn/winter), the ITCZ migrates northwards (southwards) expanding the negative
468 (positive) wind stress curl and an anomalous cyclonic (anticyclonic) circulation in the
469 western tropical South Atlantic, shoaling (deepening) the thermocline north of the sSEC
470 bifurcation, while pushing the zero wind stress curl line and the sSEC bifurcation
471 southwards (northwards) (Rodrigues et al. 2007).

472 This seasonal mechanism can be applied to the orbital-scale. In the minimum
473 precession case (boreal summer insolation maximum), the ITCZ shifts northward and
474 consequently a large-scale anomaly of negative wind stress curl associated with an
475 anomalous cyclonic circulation develops in the tropical South Atlantic as simulated in our
476 CESM1.2 experiments (Fig. 4a and b). This cyclonic circulation leads to enhanced
477 Ekman suction in the tropics, shoaling the main thermocline and forcing the southward
478 displacement of the sSEC bifurcation and hence of the SASG northern edge (Fig. 7).
479 Considering that core GL-1180 is located at ~8° S, this site is sensitive to variations in
480 the latitude of the sSEC bifurcation (Fig. 1). Therefore, during periods of boreal summer
481 insolation maximum (precession minima), the warm subsurface waters of the SASG
482 move southward of the latitude of core GL-1180 as the thermocline shoals, eventually
483 increasing upper ocean stratification north of the sSEC bifurcation (Fig. 7). The opposite
484 situation occurs during periods of precession maxima. As an example, the temperature
485 difference at 250 m water depth between two temperature profiles (Locarnini et al.,
486 2013), slightly to the north (6.5°S) and south (12.5°S) of GL-1180, is 3.6°C (Fig. S7).
487 This supports our argument that shifting the northernmost SASG limit would significantly
488 affect the main thermocline temperature at the site of GL-1180.

489 The mechanism presented here does not invalidate the role of WAM-modulated
490 trade winds zonality in piling up waters in the WTA. However, we argue that this
491 mechanism alone is insufficient to explain significant temperature changes at ~250 m
492 water depth, as presented in our study.

493

Figure 7.

5.3. Does precession-driven WTA stratification have implications for cross-equatorial transport and AMOC strength?

Since the WTA circulation is part of the upper limb of the AMOC (Zhang et al. 2011; Yang 1999), our data and the proposed mechanism for changes in upper WTA stratification may have implications for orbital-scale cross-equatorial heat and salt transport in the Atlantic.

Studies show that the rate of deep-water formation in the North Atlantic is out of phase with precession minima (Lisiecki, 2014; Lisiecki et al. 2008), that is, the AMOC seems to be weaker during boreal summer insolation maxima. However, the mechanism whereby AMOC responds to precession is still not clear (Toggweiler and Lea 2010; Lisiecki et al. 2008). Here, we propose that periods of high WTA stratification (precession minima) could be related to a decrease in the northward transport of warm and salty upper ocean waters. Ultimately, this would result in the propagation of precessional-modulated tropical variability to the high latitude North Atlantic.

According to our proposed mechanism (section 5.2), during periods of high WTA stratification, warm and saline subsurface waters of the SASG are prevented from advancing towards the equator. This is supported by the low temperature and low $\delta^{18}O_{sw\text{-}ivc}$ values of the thermocline observed during periods of high WTA stratification (Figure 2). Consequently, during precession minima, the poor penetration of warm and saline SASG waters in the WTA can reduce the cross-equatorial flow towards the North Atlantic. In contrast, during precession maxima, the northward SASG expansion and the deeper WTA thermocline allows for the penetration of warm and saline subsurface waters towards the equator, increasing the cross-equatorial transport. This idea is in line with a mid-Pleistocene record of *G. truncatulinoides* (sinistral) abundance from the western tropical North Atlantic, which indicates increased (reduced) interhemispheric

water transport during precession maxima (minima) (Kaiser et al. 2019). Besides, this hypothesis agrees with the strong AMOC observed during periods of maximum precession (Lisiecki et al. 2008). Although this link between tropical and high latitudes of the North Atlantic is only theoretical, our findings reopen the discussion about the sensitivity of the AMOC not only to boreal high latitude summer insolation (Imbrie et al. 1992) but also to tropical forcing (McIntyre and Molfino, 1996).

6. Conclusions

$\delta^{18}O$ and Mg/Ca records of planktonic foraminifera species from core GL-1180 collected in the WTA show robust evidence of precessionally modulated upper ocean stratification changes in the WTA over the last 300 ka. The precessional pace is more strongly expressed in the main thermocline rather than the surface ocean. We propose a new mechanism that explains changes in upper WTA stratification by changes in low latitude insolation. During periods of high boreal summer insolation (precession minimum), the development of an anomalous cyclonic circulation over the tropical South Atlantic due to the northward shift of the ITCZ shoals the thermocline at the equator and forces the southward migration of the SASG northern boundary. This situation shoals the main thermocline of the WTA while prevents the transport of warm and saline subsurface waters of the SASG towards the equatorial Atlantic, increasing the WTA upper ocean stratification. Finally, we hypothesize that strong WTA stratification during precession minima reduces the cross-equatorial transport of heat and salt, which may weaken the AMOC, although this connection would require further investigation.

Acknowledgments

We thank the Petrobras for providing the sediment core used in this study. This study was supported by the CAPES-ASpECTO project (grant 88887.091731/2014-01) CNPq-Aspecto (grant 429767/2018-8), CAPES-PRINT CLIMATE Project (grant 88887.310301/2018-00) and CNPq Project RAiN (grant 406322/2018-0). R. A

Nascimento acknowledges the scholarship from CAPES (grant 88887.176103/2018-00). CAPES also financially supported I.M.V. with a scholarship (grant 88887.156152/2017-00). C.M.C. acknowledges the financial support from FAPESP (grants 2018/15123-4 and 2019/24349-9), CAPES (grants 564/2015 and 88881.313535/2019-01), CNPq (grant 312458/2020-7), and the Alexander von Humboldt Foundation. ALSA is a senior scholar CNPq (grant 302521/2017-8). We also acknowledge the partial support from the Coordenação de Aperfeiçoamento de Pessoal de Nível Superior – Brasil (CAPES) – Finance Code 001. This is LSCE publication number 7665. All data presented in this manuscript are available at https://doi.org/10.1594/PANGAEA.921841.

References

Ballalai, J.M., Santos, T.P., Lessa, D.O., Venancio, I.M., Chiessi, C.M., Johnstone, H.J.H., Kuhnert, H., Claudio, M.R., Toledo, F., Costa, K.B., Albuquerque, A.L.S., 2019. Tracking spread of the Agulhas leakage into the western South atlantic and its northward transmission during the last interglacial. *Paleoceanography and Paleoclimatology.* 34(11), 1744-1760. https://doi.org/10.1029/2019PA003653;

Barker, S., Greaves, M., & Elderfield, H. (2003). A study of cleaning procedures used for foraminiferal Mg/Ca paleothermometry. *Geochemistry, Geophysics, Geosystems*, *4*(9), 1–20. https://doi.org/10.1029/2003GC000559;

Berger, A. L., Loutre, M. F., & Mélice, J. L. (2006). Equatorial insolation: From precession harmonics to eccentricity frequencies. *Climate of the Past*, 2(4), 519–533. http://doi.org/10.5194/cpd-2-519-2006;

Berger, A., & Loutre, M. F. (1997). Intertropical latitudes and half-precessional cycles. *Science*, 278, 1476-1478. https://doi.org/10.1126/science.278.5342.1476;

Berger, A., Loutre, M. F., & Tricot, C. (1993). Insolation and Earth's orbital periods. *Journal of Geophysical Research*, 98(D6). https://doi.org/10.1029/93jd00222;

574 Birch, H., Coxall, H.K., Pearson, P.N., Kroon, D., O'Regan, M., 2013. Planktonic
575 foraminifera stable isotopes and water column structure: disentangling ecological
576 signals. *Marine Micropaleontology*. 101, 127–145.
577 https://doi.org/10.1016/j.marmicro.2013.02.002;

578 Blaauw, M., & Christen, J. A. (2011). Flexible paleoclimate age-depth models using an
579 autoregressive gamma process. *Bayesian Analysis*, 6(3), 457–474.
580 https://doi.org/10.1214/11-BA618;

581 Cheng, H., Lawrence Edwards, R., Sinha, A., Spötl, C., Yi, L., Chen, S., Zhang, H.
582 (2016). The Asian monsoon over the past 640,000 years and ice age terminations.
583 *Nature*, *534*(7609), 640–646. https://doi.org/10.1038/nature18591;

584 Clement, A. C., Hall, A., & Broccoli, A. J. (2004). The importance of precessional signals
585 in the tropical climate. *Climate Dynamics*, *22*(4), 327–341.
586 https://doi.org/10.1007/s00382-003-0375-8;

587 COHMAP Members, (1988). Climatic Changes of the Last 18,000 Years: Observations
588 and model simulations. *Science*, *241*, 1043–1052;

589 Crivellari, S., Viana, P.J., Campos, M.C., Kuhnert, H., Barros, A., Cruz, F.W., Chiessi,
590 C.M., (2021). Development and characterization of a new in-house reference material
591 for stable carbon and oxygen isotopes analyses. Journal of Analytical Atomic
592 Spectrometry. DOI 10.1039/D1JA00030F

593 Elderfield, H., Vautravers, M., & Cooper, M. (2002). The relationship between shell size
594 and Mg/Ca, Sr/Ca, δ 18 O, and δ 13 C of species of planktonic foraminifera.
595 *Geochemistry, Geophysics, Geosystems*, *3*(8), 1–13.
596 https://doi.org/10.1029/2001gc000194;

597 Govin, A., Capron, E., Tzedakis, P. C., Verheyden, S., Ghaleb, B., Hillaire-Marcel, C., et
598 al. (2015). Sequence of events from the onset to the demise of the Last Interglacial:
599 Evaluating strengths and limitations of chronologies used in climatic archives.
600 *Quaternary Science Reviews*, 129, 1–36.
601 http://doi.org/10.1016/j.quascirev.2015.09.018;

602 Hagelberg, T. K., G. Bond, and P. deMenocal (1994). Milankovitch band forcing of sub-
603 Milankovitch climate variability during the Pleistocene, *Paleoceanography*, 9, 545,
604 doi:10.1029/94PA00443.

605 Hammer, Ø., Harper, D. A. T., & Ryan, P. D. (2001). PAST: Paleontological statistics
606 software package for education and data analysis. *Palaeontologia Electronica*, 76(4), 1–
607 9. http://doi.org/10.1016/j.bcp.2008.05.025;

608 Hazeleger, W., & S. Drijfhout (2006). Subtropical cells and meridional overturning
609 circulation pathways in the tropical Atlantic, *Journal of geophysical research*, 111,
610 C03013, doi:10.1029/2005JC002942;

611 Hou, A., Bahr, A., Schmidt, S., Strebl, C., Albuquerque, A. L., Chiessi, C. M., & Friedrich,
612 O. (2020). Forcing of western tropical South Atlantic sea surface temperature across
613 three glacial-interglacial cycles. *Global and Planetary Change*, 188, 103150.
614 https://doi.org/10.1016/j.gloplacha.2020.103150;

615 Hut, G. (1987). Stable isotope reference samples for geochemical and hydrological
616 investigations. Report of Consultant's Group Meeting. International Atomic Energy
617 Agency (p. 42). Vienna, Austria;

618 Imbrie, J. et al., (1992). On the structure and origin of major glaciation cycles, 1, Linear
619 responses to Milankovitch forcing, *Paleoceanography*, 7(6), 701-738.
620 https://doi.org/10.1029/92PA02253;

621 Jian, Z., Wang, Y., Dang, H., Lea, D. W., Liu, Z., Jin, H. and Yin, Y. (2020). Half-
622 precessional cycle of thermocline temperature in the western equatorial Pacific and its
623 bihemispheric dynamics, *Proc. Natl. Acad. Sci*. U. S. A., 117(13), 7044–7051,
624 doi:10.1073/pnas.1915510117;

625 Kaiser, E.A., Caldwell, A., Billups, K., (2019). North Atlantic Upper-Ocean Hydrography
626 During the Mid-Pleistocene Transition Evidenced by *Globorotalia truncatulinoides*
627 Coiling Ratios. *Paleoceanogr. Paleoclimatology* 34, 658–671.
628 https://doi.org/10.1029/2018PA003502

629 Kutzbach, J. E., & Guetter, P. J. (1986). The influence of changing orbital parameters
630 and surface boundary conditions on climate simulations for the past 18 000 years.
631 *Journal of the Atmospheric Sciences*, *45*(10), 1726–1759;

632 Kutzbach, J. E., & Liu, Z. (1997). Response of the African monsoon to orbital forcing and
633 ocean feedbacks in the middle Holocene. *Science*, *278*(5337), 440–443.
634 https://doi.org/10.1126/science.278.5337.440;

635 Kutzbach, J. E., & Otto-Bliesner, B. L. (1982). The sensitivity of the African- Asian
636 monsoonal climate to orbital parameter changes for 9000 years B.P. in a low-resolution
637 general circulation model. *Journal of the Atmospheric Sciences*.
638 https://doi.org/10.1175/1520 0469(1982)039<1177:TSOTAA>2.0.CO;2;

639 Laskar, J., Robutel, P., Joutel, F., Gastineau, M., Correia, A.C.M., Levrard, B. (2004). A
640 long-term numerical solution for the insolation quantities of the Earth. *Astronomy and*
641 *Astrophysics*, 428, 261-285. https://doi.org/10.1051/0004-6361:20041335;

642 Lisiecki, L. E., & Raymo, M. E. (2005). A Pliocene-Pleistocene stack of 57 globally
643 distributed benthic δ 18O records. *Paleoceanography*, *20*(1), 1–17.
644 https://doi.org/10.1029/2004PA001071;

Lisiecki, L. E., Raymo, M. E., & Curry, W. B. (2008). Atlantic overturning responses to Late Pleistocene climate forcings. *Nature*, *456*(7218), 85–88. https://doi.org/10.1038/nature07425;

Lisiecki, L.E., (2014). Atlantic overturning responses to obliquity and precession over the last 3 Myr. *Paleoceanography* 29, 71–86. https://doi.org/10.1002/2013PA002505

Locarnini, R. A., Mishonov, A. V., Antonov, J. I., Boyer, T. P., Garcia, H. E., Baranova, O. K., et al. (2013). World Ocean Atlas 2013, Volume 1: Temperature. In S. Levitus & A. Mishonov (Eds.), NOAA Atlas NESDIS 73 (p. 40). Silver Spring, MD: U.S. Government Printing Office;

Lumpkin, R., & Speer, K. (2003). Large-scale vertical and horizontal circulation in the North Atlantic Ocean. *Journal of Physical Oceanography*, *33*, 1902–1920. https://doi.org/10.1175/1520-0485(2003)033%3C1902:LVAHCI%3E2.0.CO;2;

Luyten, J., J. Pedlosky,and H. Stommel (1993b). Climatic inferences from the ventilated thermocline, *Climatic Change*, 5, 183-191. 10.1007/BF02423489;

Luyten, J.R., Pedlosky, J., Stommel, H., (1983a). The ventilated thermocline. *Journal of Physical Oceanography*, 13, 292-309. https://doi.org/10.1175/1520 0485(1983)013<0292:TVT>2.0.CO;2;

Mantsis, D. F., Clement, A., Broccoli, A., Erb, M. (2011). Climate feedbacks in response to changes in obliquity. *Journal of Climate*, 24, 2830–2845. https://doi.org/10.1175/2010JCLI3986.1;

Mantsis, D. F., Lintner, B. R., Broccoli, A. J., Erb, M. P., Clement, A. C., & Park, H. S. (2014). The response of large-scale circulation to obliquity-induced changes in meridional heating gradients. *Journal of Climate*, 27(14), 5504–5516. https://doi.org/10.1175/JCLI-D-13-00526.1;

669 Marcello, F., Wainer, I., & Rodrigues, R. R. (2018). South Atlantic Subtropical Gyre late
670 twentieth century changes. *Journal of Geophysical Research: Oceans*, 123, 5194–5209.
671 https://doi.org/10.1029/2018JC013815;

672 Marshall, J., Donohoe, A., Ferreira, D., McGee, D. (2014). The ocean's role in setting the
673 mean position of the Inter-Tropical Convergence Zone. *Climate Dynamics*, *42*(7–8),
674 1967–1979. https://doi.org/10.1007/s00382-013-1767-z;

675 McIntyre, A., & Molfino, B. (1996). Forcing of Atlantic equatorial and subpolar millennial
676 cycles by precession. *Science*, *274*(13), 1867–1870;

677 McIntyre, A., Ruddiman, W. F., Karlin, K., & Mix, A. C. (1989). Surface water response
678 of the equatorial Atlantic Ocean to orbital forcing. *Paleoceanography*, *4*(1), 19–55.
679 https://doi.org/10.1029/PA004i001p00019;

680 Molfino, B., & Mcintyre, A. (1990). Precessional forcing of nutricline dynamics in the
681 equatorial Atlantic. *Science*, *249*(4970), 766–769.
682 https://doi.org/10.1126/science.249.4970.766;

683 Mulitza, S., Dürkoop, A., Hale, W., Wefer, G., & Niebler, H. S. (1997). Planktonic
684 foraminifera as recorders of past surface-water stratification. *Geology*, *25*(4), 335–338.
685 https://doi.org/10.1130/0091-7613(1997)025<0335:PFAROP>2.3.CO;2;

686 Niemitz, M.D. and Billups, K., (2005). Millennial-scale variability in western tropical
687 Atlantic surface ocean hydrography during the early Pliocene. *Marine*
688 *Micropaleontology*, *54*(3-4),pp.155-166. https://doi.org/10.1016/j.marmicro.2004.10.001

689 Poole, R., & Tomczak, M. (1999). Optimal multiparameter analysis of the water mass
690 structure in the Atlantic Ocean thermocline. *Deep Sea Research Part I: Oceanographic*
691 *Research Papers*, *46* (11), 1895-1921. https://doi.org/10.1016/S0967-0637(99)00025-4;

692 Regenberg, M., Steph, S., Nürnberg, D., Tiedemann, R., & Garbe-Schönberg, D. (2009).
693 Calibrating Mg/Ca ratios of multiple planktonic foraminiferal species with δ18O-
694 calcification temperatures: Paleothermometry for the upper water column. *Earth and*
695 *Planetary Science Letters*, *278*(3–4), 324–336.
696 https://doi.org/10.1016/j.epsl.2008.12.019;

697 Reimer, P. J., Bard, E., Bayliss, A., Beck, J. W., Blackwell, P. G., Ramsey, C. B., et al.
698 (2013). IntCal13 and Marine13 radiocarbon age calibration curves 0–50,000 years cal
699 BP. *Radiocarbon*, 55(04), 1869–1887. https://doi.org/10.2458/azu_js_rc.55.16947;

700 Rodrigues, R. R., Rothstein, L. M., & Wimbush, M. (2007). Seasonal variability of the
701 South Equatorial Current bifurcation in the Atlantic Ocean: A numerical study. *Journal of*
702 *Physical Oceanography*, *37*(1), 16–30. https://doi.org/10.1175/JPO2983.1;

703 Rutherford, S., D'Hondt. (2000). Early onset and tropical forcing of 100,000-year
704 Pleistocene glacial cycles. Nature, 408, 71-75. https://doi.org/10.1038/35040533;

705 Santos, T.P., Ballalai, J.M., Franco, D.R., Oliveira, R.R., Lessa, D.O., Venancio, I.M.,
706 Chiessi, C.M., Kuhnert, H., Johnstone, H., Albuquerque, A.L.S. (2020). Asymmetric
707 response of the subtropical western South Atlantic thermocline to the Dansgaard-
708 Oeschger events of Marine Isotope Stages 5 and 3. *Quaternary Science Reviews*, 236.
709 https://doi.org/10.1016/j.quascirev.2020.106307

710 Santos, T.P., Lessa, D.O., Venancio, I.M., Chiessi, C.M., Mulitza, S., Kuhnert, H., Govin,
711 A., Machado, T., Costa, K.B., Toledo, F., Dias, B.B., Albuquerque, A.L.S. (2017a).
712 Prolonged warming of the Brazil Current precedes deglaciations. *Earth and Planetary*
713 *Science Letters,* 463, 1-12. https://doi.org/10.1016/j.epsl.2017.01.014.

714 Santos, T.P., Lessa, D.O., Venancio, I.M., Chiessi, C.M., Mulitza, S., Kuhnert, H.,
715 Albuquerque, A.L.S. (2017b). The impact of the AMOC resumption in the western

South Atlantic thermocline at the onset of the Last Interglacial. *Geophysical Research Letters*, 44. https://doi.org/10.1002/2017GL074457.

Schlitzer, R. (2017). Ocean Data View, odv.awi.de;

Schneider, T., Bischoff, T., & Haug, G. H. (2014). Migrations and dynamics of the intertropical convergence zone. *Nature*, *513*(7516), 45–53. https://doi.org/10.1038/nature13636;

Schott, F. A., M. Dengler, R. Zantopp, L. Stramma, J. Fischer, and P. Brandt (2005), The shallow and deep western boundary circulation of the South Atlantic at 5°–11°S, *Journal of Physical Oceanography*, 35, 2031–2053. https://doi.org/10.1175/JPO2813.1

Schott, F., J. Fischer, and L. Stramma, (1998). Transports and pathways of the upper-layer circulation in the western tropical Atlantic, *Journal of Physical Oceanography*, 28, 1904–1928. https://doi.org/10.1175/1520-0485(1998)028<1904:TAPOTU>2.0.CO;2**;**

Schulz, M., & Mudelsee, M. (2002). REDFIT: Estimating red-noise spectra directly from unevenly spaced paleoclimatic time series. *Computers and Geosciences*, 28(3), 421–426. http://doi.org/10.1016/S0098-3004(01)00044-9;

Scussolini, P., Marino, G., Brummer, G.-J. A., & Peeters, F. J. C. (2015). Saline Indian Ocean waters invaded the South Atlantic thermocline during glacial termination II. *Geology*, 43(2), 139–142. https://doi.org/10.1130/G36238.1;

Shackleton, N. J. (1974). Attainment of isotopic equilibrium between ocean water and the benthonic foraminifera geuns *Uvigerina*: Isotopic changes in the ocean during the last glacial. *Colloques Internationaux Du C.N.R.S.*, *219*, 203–210;

739 Skonieczny, C., McGee, D., Winckler, G., Bory, A., Bradtmiller, L. I., Kinsley, C. W., et
740 al., (2019). Monsoon-driven Saharan dust variability over the past 240,000 years.
741 *Science Advances*, *5*(1), 1–9. https://doi.org/10.1126/sciadv.aav1887;

742 Spratt, R. M., & Lisiecki, L. E. (2016). A Late Pleistocene sea level stack. *Climate of the*
743 *Past*, *12*(4), 1079–1092. https://doi.org/10.5194/cp-12-1079-2016;

744 Sprintall, J., & Tomczak, M., (1993). On the formation of Central Water and thermocline
745 ventilation in the southern hemisphere. *Deep-Sea Research.* 40, 827-848.
746 https://doi.org/10.1016/0967-0637(93)90074-D;

747 Steele, M., Morley, R., Ermold, W. (2001). PHC: A global ocean hydrography with a high-
748 quality Arctic Ocean. *Journal of Climate*, *14*(9), 2079-2087.
749 https://doi.org/10.1175/1520-0442(2001)014<2079:PAGOHW>2.0.CO;2;

750 Stramma, L. (1991). Geostrophic transport of the South Equatorial Current in the Atlantic.
751 *Journal of Marine Research*, *49*(2), 281–294.
752 https://doi.org/10.1357/002224091784995864;

753 Stramma, L., & England, M. (1999). On the water masses and mean circulation of the
754 South Atlantic Ocean. *Journal of geophysical research*, v. 104, p. 20.863-20.883.
755 https://doi.org/10.1029/1999JC900139;

756 Timmermann, A., Friedrich, T., Timm, O. E., Chikamoto, M. O., Abe-Ouchi, A., &
757 Ganopolski, A. (2014). Modeling obliquity and CO2 effects on southern hemisphere
758 climate during the past 408 ka. *Journal of Climate*, *27*(5), 1863–1875.
759 https://doi.org/10.1175/JCLI-D-13-00311.1;

760 Toggweiler, J. R., & Lea, D. W. (2010). Temperature differences between the
761 hemispheres and ice age climate variability. *Paleoceanography*, *25*, 1–14.
762 https://doi.org/10.1029/2009PA001758;

763 Vellinga, M., & Wu, P. (2004). Low-latitude freshwater influence on centennial variability
764 of the Atlantic thermohaline circulation. *Journal of Climate*, *17*(23), 4498–4511.
765 https://doi.org/10.1175/3219.1;

766 Venancio, I. M., Mulitza, S., Govin, A., Santos, T. P., Lessa, D. O., Albuquerque, A. L.
767 S., et al. (2018). Millennial- to orbital-scale responses of Western Equatorial Atlantic
768 thermocline depth to changes in the trade wind system since the last interglacial.
769 *Paleoceanography and Paleoclimatology*, *33*(12), 1490–1507.
770 https://doi.org/10.1029/2018PA003437;

771 Wolff, T., Mulitza, S., Rtihlemann, C., & Wefer, G. (1999). Response of the tropical
772 Atlantic thermocline to late Quaternary trade wind changes. *Paleoceanography*, *14*(3),
773 374–383. https://doi.org/10.1029/1999PA900011;

774 Yang, J. (1999). A linkage between decadal climate variations in the Labrador Sea and
775 the tropical Atlantic Ocean. *Geophysical Research Letters*, *26*(8), 1023–1026.
776 https://doi.org/10.1029/1999GL900181;

777 Zhang, D., Msadek, R., McPhaden, M. J., & Delworth, T. (2011). Multidecadal variability
778 of the North Brazil Current and its connection to the Atlantic meridional overturning
779 circulation. *Journal of Geophysical Research*, *116*(C4), 1–9.
780 https://doi.org/10.1029/2010jc006812;

781 Zhang, Y., Chiessi, C. M., Mulitza, S., Zabel, M., Trindade, R. I. F., Hollanda, M. H. B.
782 M., DantasDantas, E.L., Govin A., Tiedemann, R., Wefer, G. (2015). Origin of increased
783 terrigenous supply to the NE south American continental margin during Heinrich Stadial
784 1 and the younger Dryas. *Earth and Planetary Science Letters*, 432, 493–500.
785 http://doi.org/10.1016/j.epsl.2015.09.054.

786 Zweng, M.M, J.R. Reagan, J.I. Antonov, R.A. Locarnini, A.V. Mishonov, T.P. Boyer, H.E.
787 Garcia, O.K. Baranova, D.R. Johnson, D.Seidov, M.M. Biddle, (2013). *World Ocean*

Atlas 2013, Volume 2: Salinity. S. Levitus, Ed., A. Mishonov Technical Ed.; NOAA Atlas NESDIS 74, 39 pp.

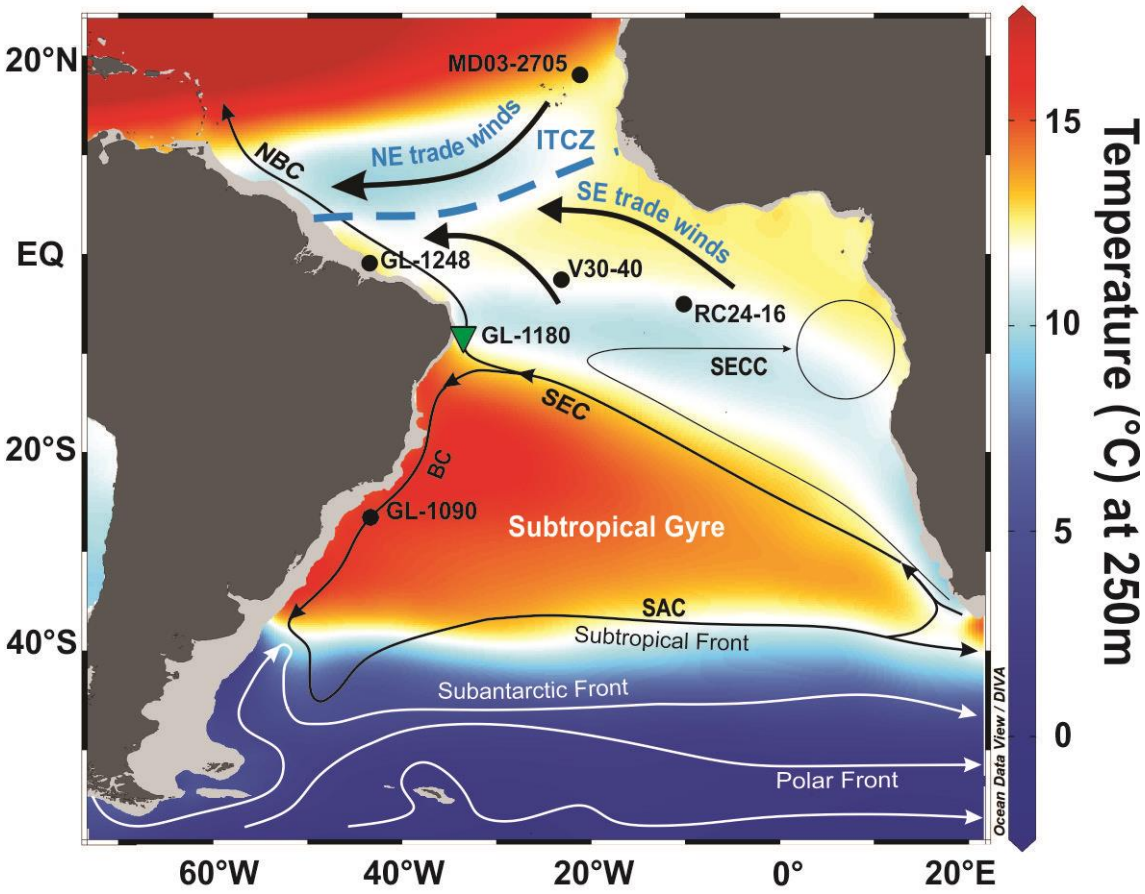

Figure 1. Location of the sediment core GL-1180 analyzed in this study (green triangle) and other cores used in the discussion (black dots): GL-1090 (Santos et al. 2020; Ballalai et al. 2019; Santos et al. 2017a,b); GL-1248 (Venancio et al. 2018); MD03-2705 (Skonieczny et al. 2019); V30-40 and RC24-16 (McIntyre et al. 1989);. The color scale depicts annual temperature at 250 m water depth (Locarnini et al., 2013). The dashed blue line represents the average position of the Intertropical Convergence Zone position (ITCZ). Thick black arrows indicate the trade winds. Thin black arrows show the main wind-driven upper ocean circulation. BC: Brazil Current; NBC: North Brazil Current; SAC: South Atlantic Current; SECC: South Equatorial Counter-Current; SEC: South Equatorial Current. White thin arrows represent the Antarctic Circumpolar Current. The figure was generated using the software Ocean Data View (Schlitzer, 2017).

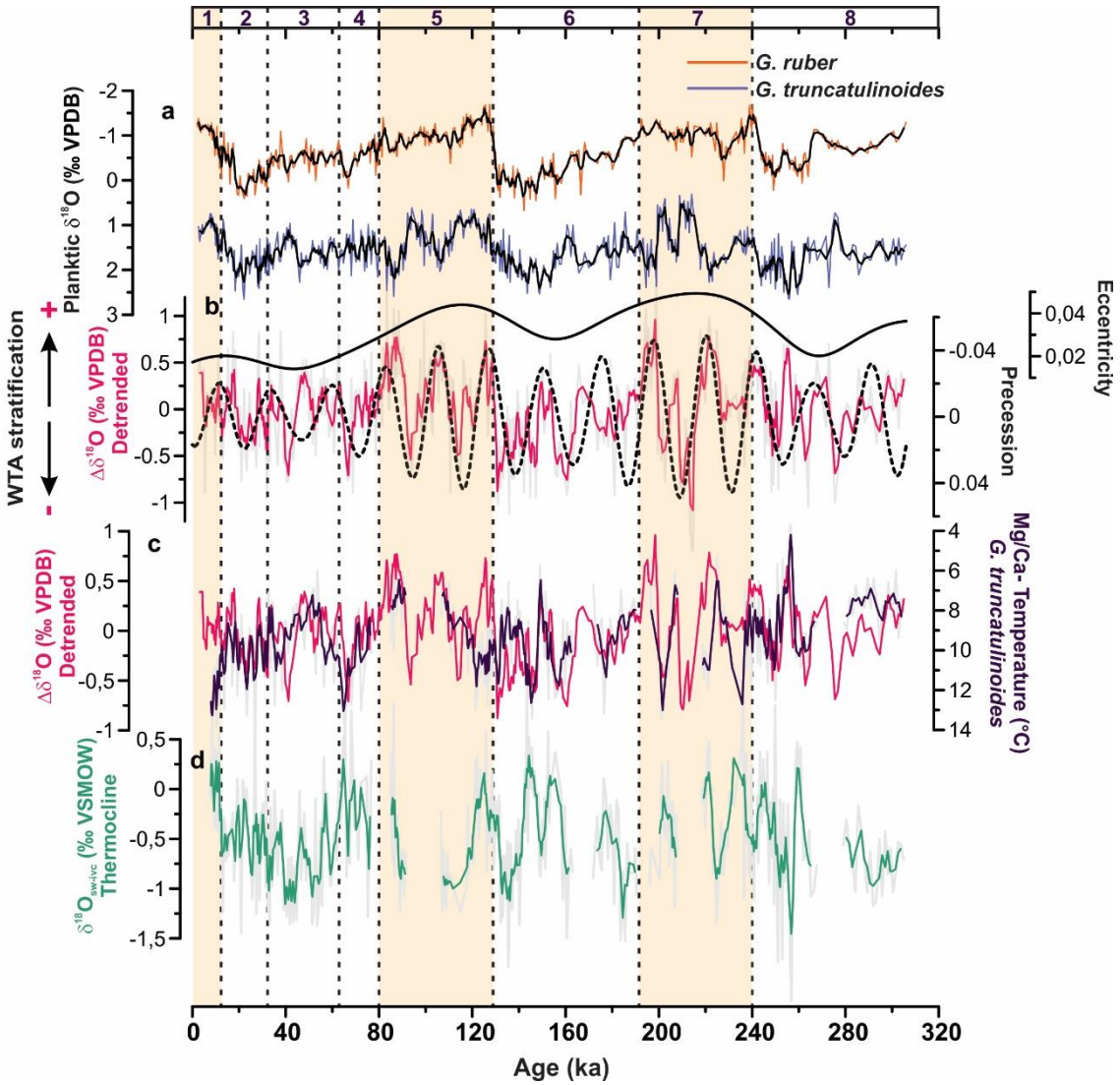

Figure 2. Stable oxygen isotopes ($\delta^{18}O$), Mg/Ca-based temperatures and derived data ($\Delta\delta^{18}O$ and $\delta^{18}O$ of seawater) from sediment core GL-1180 together with orbital parameters. a) $\delta^{18}O$ of *Globigerinoides ruber* (orange) and *Globorotalia truncatulinoides* (dark blue) with 3-points running averages (black); b) linearly detrended $\Delta\delta^{18}O$ ($\delta^{18}O_{G.\ truncatulinoides}$ - $\delta^{18}O_{G.\ ruber}$) (light grey line) with 3-points running average (pink); the black continuous line represents eccentricity and the black dashed line shows precession; c) Mg/Ca-based temperatures obtained from *G. truncatulinoides* (light grey line) with 3-points running average (purple) and 3-points running average of linearly detrended $\Delta\delta^{18}O$ (light pink); note that the temperature axis is inverted; d) main thermocline ice-volume-corrected $\delta^{18}O$ of seawater ($\delta^{18}O_{sw\text{-}ivc}$) as a proxy for relative changes in main thermocline salinity (light grey line) with 3-points running average (green). Values were reconstructed from the $\delta^{18}O$ and Mg/Ca-based temperature of *G. truncatulinoides*. Numbers at the top x-axis indicate Marine Isotope Stages (MIS), while colored bars denote interglacial periods.

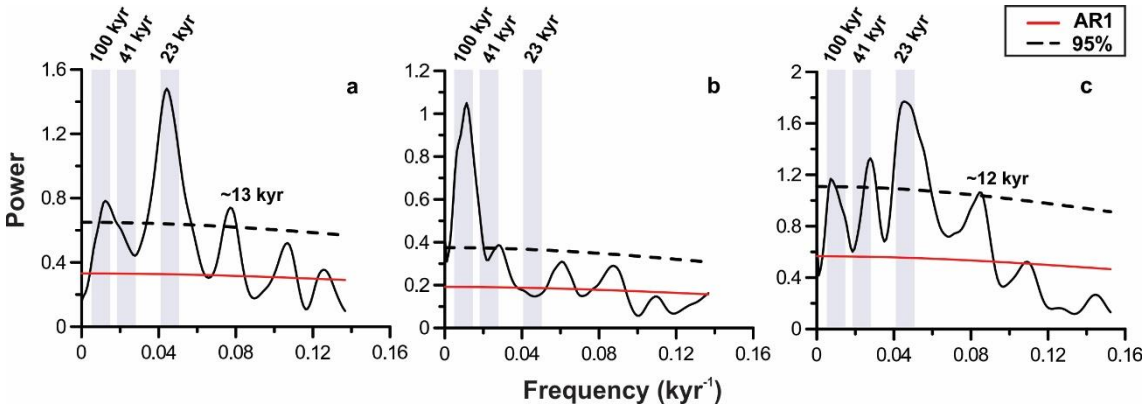

827

828 **Figure 3.** Time-series analyses performed on planktonic $\delta^{18}O$ corrected for changes in
829 ice-volume ($\delta^{18}O_{ivc}$) (see section 3.6) and $\Delta\delta^{18}O$ from sediment core GL-1180. a)
830 *Globorotalia truncatulinoides* $\delta^{18}O_{ivc}$; b) *Globigerinoides ruber* $\delta^{18}O_{ivc}$; c) $\Delta\delta^{18}O$
831 calculated as $\delta^{18}O_{G.\ truncatulinoides} - \delta^{18}O_{G.\ ruber}$. The red line (AR1) represents the red noise
832 spectrum, and the dashed line represents the false alarm level at 95%. The REDFIT
833 algorithm (Schulz & Mudelsee 2002) was used to perform the analyses. The light grey
834 bars highlight the bands of eccentricity, obliquity, and precession.
835
836

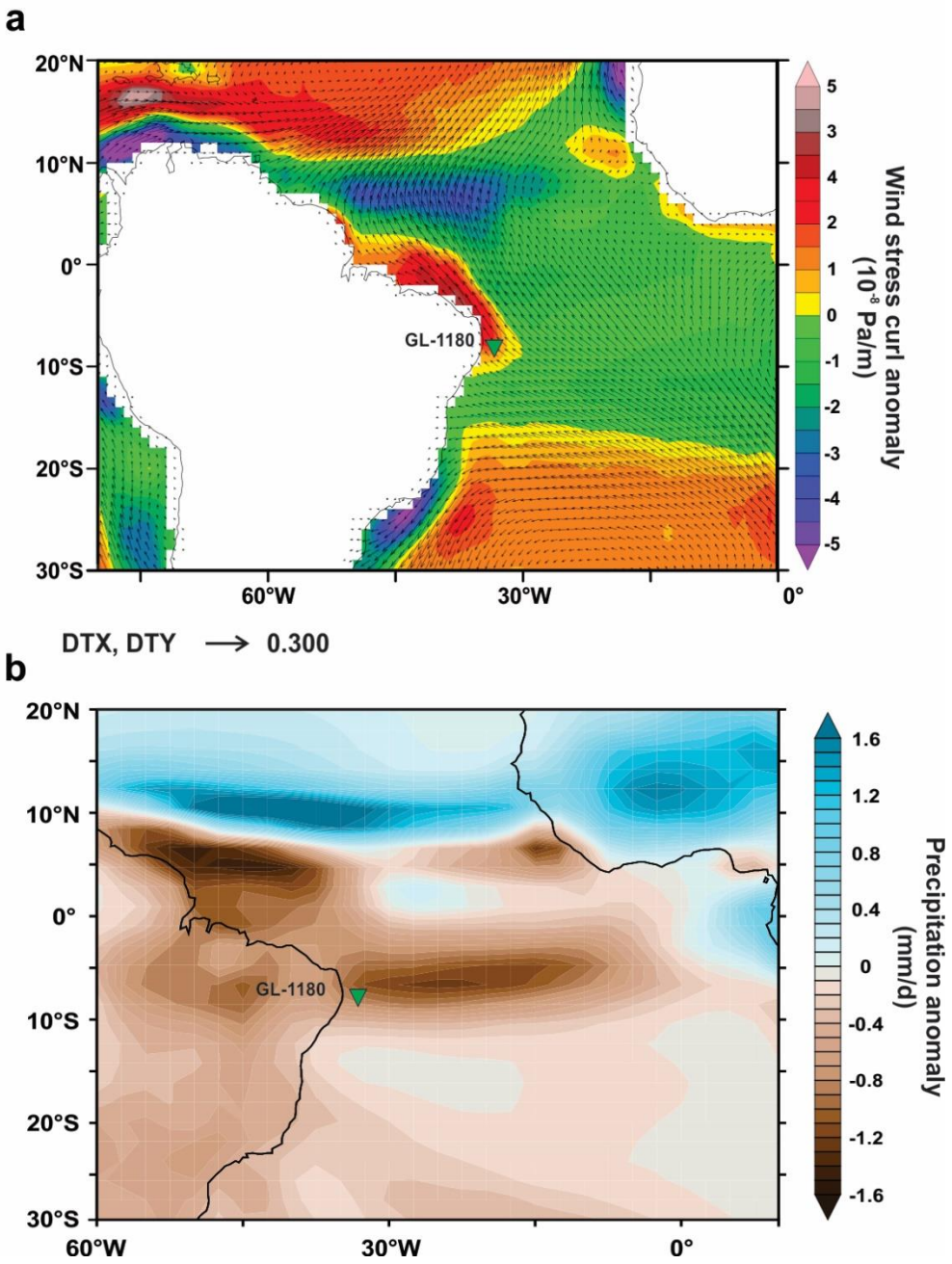

Figure 4. Effect of precession on annual mean anomaly (experiment P_min minus P_max) of wind stress and precipitation as simulated by CESM1.2. a) Wind stress anomaly. Arrows indicate the modeled wind stress (Pa) anomaly. Colors show the difference in wind stress curl (in units of 10^{-8} Pa/m). In the Southern Hemisphere, negative values (cool colors) indicate anomalous cyclonic circulation (divergence), while positive values (warm colors) indicate anomalous anticyclonic circulation (convergence). b) Precipitation anomaly. Colors show the precipitation anomaly (in units of mm/d). Positive (negative) values indicate anomalous increase (decrease) in precipitation.

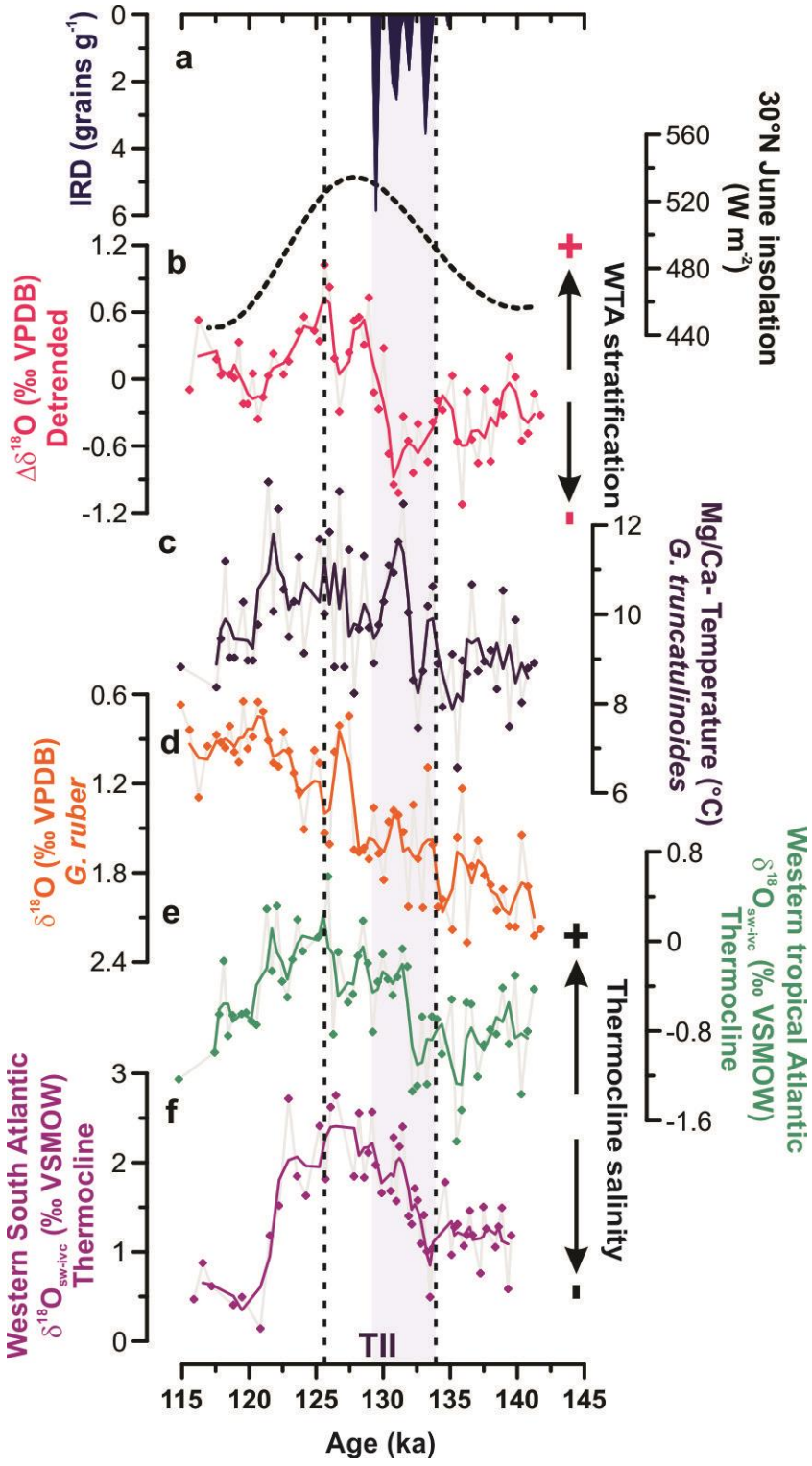

Figure 5. WTA upper ocean stratification and thermocline temperature around Termination II (TII). a) Ice-rafted debris (IRD) from ODP Site 1063 (Deaney et al., 2017); b) 3-points running average of linearly detrended $\Delta\delta^{18}O$ (pink) and June isolation at 30° N (dotted line) (Laskar et al. 2004); c) Mg/Ca-based temperature of *G. truncatulinoides* (dark purple) from GL-1180; d) $\delta^{18}O$ of *G. truncatulinoides* (orange) with 5-points running average; e) thermocline ice-volume-corrected seawater $\delta^{18}O$ ($\delta^{18}O_{sw\text{-}ivc}$) as a proxy for relative changes in thermocline salinity (green); f) $\delta^{18}O_{sw\text{-}ivc}$ from site GL-1090 (Ballalai

et al. 2019) (light purple). The light grey bar marks Heinrich stadial 11. Data are presented in the original age model of the quoted studies.

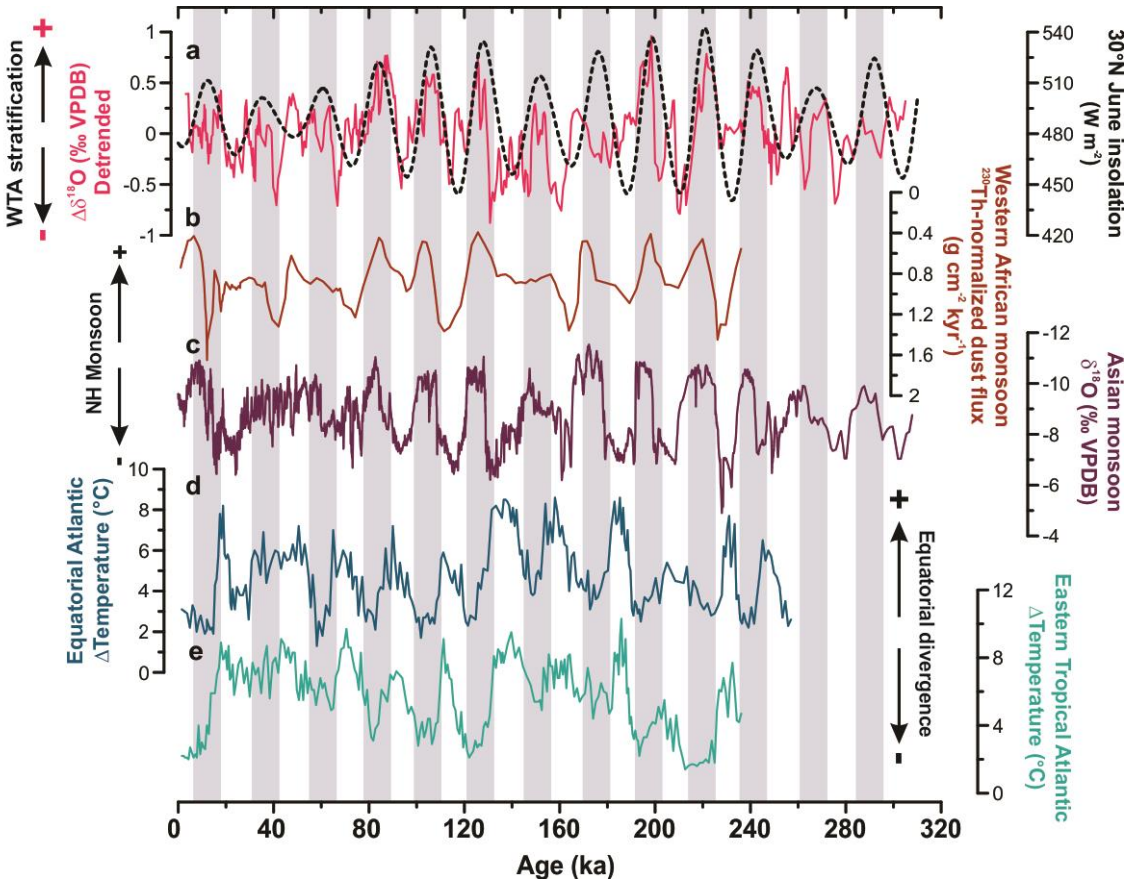

Figure 6. Comparison between $\Delta\delta^{18}O$ from GL-1180 with processional-modulated records associated with North Hemisphere monsoon systems and Tropical Atlantic divergence zone. a) 3-points running average of linearly detrended $\Delta\delta^{18}O$ (pink) from core GL-1180. The dashed line represents June insolation at 30° N (Laskar et al. 2004); b) ^{230}Th-normalized Sahara dust fluxes from sediment core MD03-2705 (brown; 3-points running average) (Skonieczny et al. 2019); c) speleothem $\delta^{18}O$ record of Asian monsoon system (dark purple) (Cheng et al. 2016); d) Equatorial Atlantic seasonal Δtemperature record (summer temperature – winter temperature) based on transfer function (site V30-40) (blue) and e) same as d in the eastern tropical Atlantic (ETA) (site RC24-16) (cyan) (McIntyre et al. 1989). High ΔT indicates strong ETA divergence. Grey bars are aligned with high boreal summer insolation at 30° N. All data are presented in the original age model of the quoted studies.

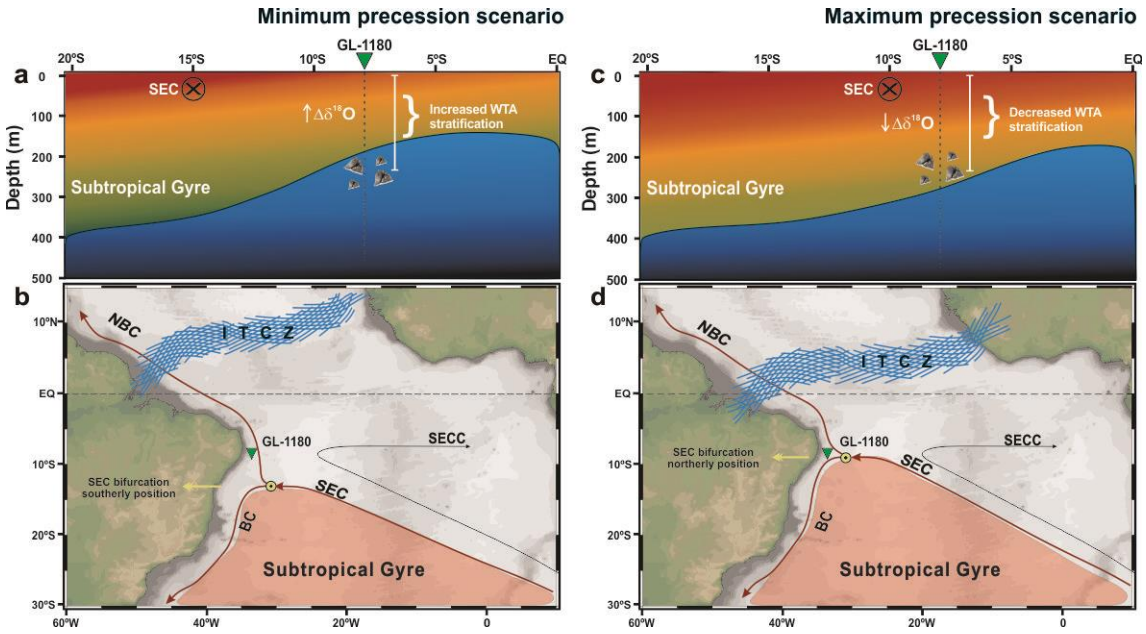

Figure 7. Schematic representation of the South Equatorial Current (SEC), South Atlantic Subtropical Gyre (SASG) and Intertropical Convergence Zone (ITCZ) latitudinal displacement, together with changes in thermocline stratification during minimum (left panels) and maximum (right panels) precession scenarios. Upper panels) Schematic zonal sections of the tropical South Atlantic illustrating the vertical displacement of the main thermocline and intrusion of SASG waters towards the equator during a) minimum precession (boreal summer at perihelion) and c) maximum precession (boreal summer at aphelion). Lower panels) Schematic map of the latitudinal displacement of the SEC and the SASG relative to the position of sediment core GL-1180 during b) minimum precession and d) maximum precession. Warm and cool colors in the upper panels indicate warm and cold waters, respectively. Background colors are illustrative. BC: Brazil Current, NBC: North Brazil Current, SECC: South Equatorial Counter Current.